Marangoni flows during nonsolvent induced phase separation

Douglas R. Tree,*,† Tatsuhiro Iwama,‡ Kris T. Delaney,¶ Joshua Lee,§ and Glenn H. Fredrickson‖

†*Chemical Engineering Department, Brigham Young University, Provo, UT 84602*
‡*Asahi Kasei Corporation, 2-1 Samejima, Fuji, Shizuoka 416-8501 Japan*
¶*Materials Research Laboratory, University of California, Santa Barbara, CA 93106-5121*
§*Chemical Engineering Department, University of California, Santa Barbara, CA 93106-5121*
‖*Chemical Engineering Department, Materials Department and Materials Research Laboratory, University of California, Santa Barbara, CA 93106-5121*

E-mail: tree.doug@byu.edu

Abstract

Motivated by the much discussed, yet unexplained, presence of macrovoids in polymer membranes, we explore the impact of Marangoni flows in the process of nonsolvent induced phase separation. Such flows have been hypothesized to be important to the formation of macrovoids, but little quantitative evidence has been produced to date. Using a recently developed multi-fluid phase field model, we find that roll cells indicative of a solutal Marangoni instability are manifest during solvent/nonsolvent exchange across a stable interface. However, these flows are weak and subsequently do not produce morphological features that might lead to macrovoid formation. By contrast, initial conditions that lead to an immediate precipitation of the polymer film coincide with large Marangoni flows that disturb the interface. The presence of such flows suggests a new experimental and theoretical direction in the search for a macrovoid formation mechanism.

Non-solvent induced phase separation (NIPS) is a widely used process to create a porous microstructure in a variety of polymer materials including membranes[1] and colloidal particles[2]. As shown in Figure 1, the NIPS process for membranes consists of either immersing or co-flowing a polymer/good solvent mixture alongside a nonsolvent, inducing the phase separation of a polymer-rich phase from a polymer-lean phase. As good solvent and nonsolvent are continuously exchanged, the polymer-rich phase eventually solidifies freezing the microstructure. The resulting characteristic size, distribution and defectivity of the pore network are the primary determinant of the commercial uses and value of the material.

One common nuisance in the NIPS process is the appearance of relatively large "macrovoids" that introduce mechanical defects. Since at least the early 1970s, researchers have worked to understand how macrovoids form in an attempt to find ways to eliminate them[3,4]. However, because of the complexity of the process, most of our knowledge of macrovoid formation remains qualitative. Macrovoids are much larger than the rest of the pore network and are roughly periodically spaced. They are observed when demixing occurs very quickly—often accompanied by hydrodynamic flows—and their formation is sensitive to solvent/nonsolvent miscibility[1,5,6]. Researchers continue to debate multiple mechanisms con-

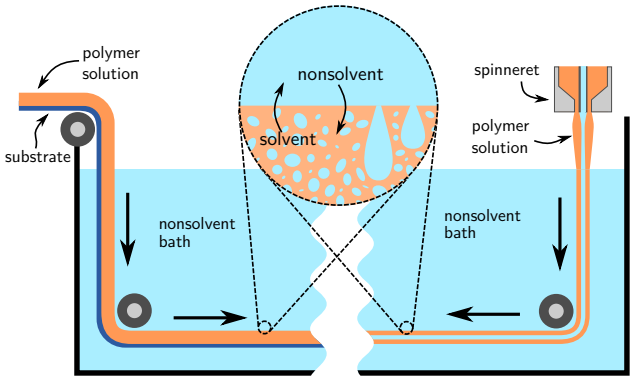

Figure 1: A schematic showing a continuous process for producing flat membranes (left) or hollow-fiber membranes (right). Membranes consist of a porous microstructure (inset) that occasionally includes unwanted, finger-like voids.

sistent with these observations; some have argued that macrovoid formation is primarily a result of the mass-transfer driven phase separation process, while others believe mechanical stresses at the film/bath interface are the primary cause[1,5–8].

We argue that a more quantitative approach is necessary to reconcile these disparate mechanisms. To this end, we recently developed a multi-fluid phase-field model capable of describing the phase-separation and hydrodynamics of an incompressible ternary polymer solution with nearly arbitrary viscosity contrast[9]. The model is given by a set of coupled diffusion, momentum and continuity equations,

$$\frac{\partial \phi_i}{\partial t} + \boldsymbol{v} \cdot \nabla \phi_i = \nabla \cdot \left[\sum_j^{p,n} M_{ij} \nabla \mu_j \right] \quad (1)$$

$$0 = -\nabla p + \nabla \cdot \left[\eta (\nabla \boldsymbol{v} + \nabla \boldsymbol{v}^T) \right] - \nabla \cdot \boldsymbol{\Pi} \quad (2)$$

$$\nabla \cdot \boldsymbol{v} = 0 \quad (3)$$

where ϕ_p and ϕ_n are, respectively, the volume fractions of the polymer and nonsolvent components, $\boldsymbol{v}$ is the velocity and p is the pressure. Additionally, the diffusive flux in Eq. 1 contains chemical potential terms, μ_i, and concentration-dependent mobility coefficients, M_{ij}.

The chemical potential is derived from a free energy functional consisting of a local Flory-Huggins expression and square gradient terms with parameters describing species molecular weight, N_i, enthalpic interactions between components, χ_{ij}, and square-gradient coefficients, κ_i. For this work, we make the simplifying assumptions that $N_p = N$, $N_n = N_s = 1$, $\chi_{pn} = \chi$, $\chi_{ps} = \chi_{ns} = 0$ and $\kappa_p = \kappa_n = \kappa$. The momentum equation, Eq. 2, contains a solution viscosity, η, which can depend on local concentration, and an osmotic stress tensor, $\boldsymbol{\Pi}$, that is directly related to chemical potential gradients. We solve the model numerically using a custom CUDA/C++ program on a GPU with a semi-implicit, pseudo-spectral method. Many more details of the model and methods can be found in the Supporting Information and in our previous work[9].

Equations 1–3 represent a non-trivial description of phase separation, diffusion and convection in a ternary polymer solution. However, our current model does not include elastic forces, and therefore cannot be used to investigate macrovoid formation via mechanical rupture[10]. Despite this deficiency, our model does allow us to quantitatively evaluate potential mechanisms for macrovoid formation driven by thermodynamic and transport processes. It should also be noted that there are alternative methods capable of simulating the hydrodynamics of phase-separating polymeric fluids including Lattice Boltzmann[11,12], dissipative particle dynamics[13], kinetic Monte Carlo[14] and multi-particle collision dynamics[15].

In this Letter we investigate the possibility that Marangoni flows, i.e. flows driven by a concentration-dependent surface tension gradient, play a key role in initiating macrovoid formation during the NIPS process. Matz, Frommer and Messalem (MFM) originally proposed that a Marangoni instability was responsible for macrovoid formation in the early 1970s[3,4], but like most theories, it remains controversial[1,5,6,16]. Indeed, to our knowledge, it has never been conclusively shown that a solutocapillary hydrodynamic instability exists in the NIPS process, nor have details of this instability been quantified sufficiently to connect them to macrovoid formation.

The requirements for a solutal Marangoni in-

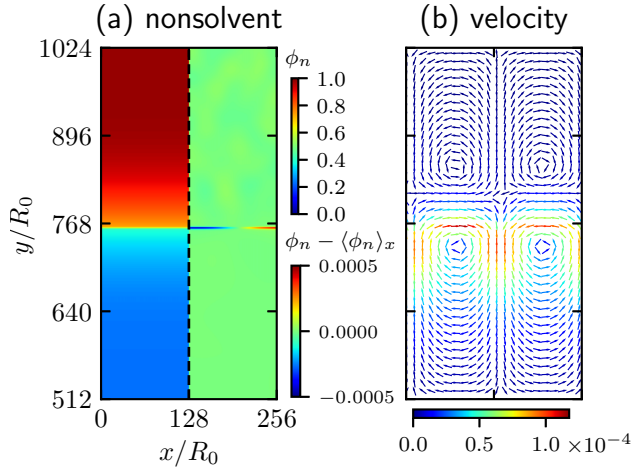

Figure 2: (a) Nonsolvent volume fraction and (b) bulk velocity at $t = 100$ for a 2D simulation of NIPS with thermodynamic parameters $N = 20$, $\chi = 1.048$, $\kappa = 2$, an initial bath composition of $\phi_p^{\text{bath}} = 0.01$, $\phi_n^{\text{bath}} = 0.98$, and an initial film composition of $\phi_p^{\text{film}} = 0.367$ and $\phi_n^{\text{film}} = 0.238$. The right half of panel (a) shows the deviation of the nonsolvent volume fraction from the x-spatial average, $\langle\phi_n\rangle_x$ for half of the simulation domain. The simulation time is in units of the Rouse time and lengths are in units of the polymer end-to-end distance R_0, which are approximately 0.1 μs and 4.5 nm respectively for a polymer at room temperature with a 1 nm statistical segment length and a solvent viscosity similar to water[9].

stability were described in a seminal paper by Sternling and Scriven[17], and include (i) an interface between two liquid phases, (ii) transport of a surfactant between the phases and (iii) an asymmetry of either diffusion or viscosity between the phases[18]. All three conditions are satisfied in a NIPS process preceding delayed precipitation, and are rigorously justified in the Supporting Information with both a theory and numerical calculations of the surface tension in our model.

Given that the basic criteria for the MFM hypothesis are satisfied, we looked for direct evidence of a Marangoni instability by simulating the NIPS process. To do so, we initialized a 2D simulation with two out-of-equilibrium phases — a nonsolvent bath and a film comprised of a mixture of polymer, solvent and nonsolvent — and observed the resulting diffusion and convection. A few comments about the details of this calculation are in order:

- The industrial NIPS process can be very complex and may include pre-treatment steps or a lengthy mass-transfer process resulting in an inhomogeneous film[19]. In lieu of imposing an *ad hoc* concentration profile, we chose homogeneous initial conditions with a polymer film concentration near the two-phase region that resulted in a delayed precipitation event. The choice of homogeneous conditions also ensures clarity when examining the effects of Marangoni flow.

- The initial concentrations were seeded with uniform random noise of magnitude $|\delta\phi| = 0.005$ about the average composition to provide an initial perturbation and to break symmetry. Such a perturbation is necessary because our model does not include thermal fluctuations, which also precludes the observation of barrier-crossing phenomena such as nucleation.

- The boundaries of the simulation box are periodic in the x-direction, and symmetry in the y-direction creates no-flux conditions (the mirror-image lower half of the simulation domain is not shown). The simulation box also has a large aspect ratio, so that the bath and film are effectively infinite over the observed simulation time.

- It is challenging to accurately model transport of a polymer solution over concentrations spanning the dilute to concentrated regimes. In these simulations, we use previously derived mutual diffusion coefficients that smoothly cross over between well-known limits, but are almost certainly inaccurate at intermediate concentrations[9].

- For clarity in examining the relevant phenomena, results were obtained with a constant viscosity $\eta = \eta_s$, appropriate for a very dilute polymer solution.

Figure 2 shows the results of a characteristic simulation soon after the initiation of diffusive exchange. The left half of Figure 2(a) shows a non-solvent concentration profile exhibiting the beginning of solvent/nonsolvent diffusion across an interface separating the two phases. The right half of Figure 2(a) shows the deviation of the non-solvent concentration from the horizontally-averaged (x-direction) value, revealing the existence of nonsolvent-rich and nonsolvent-lean regions along the interface. The bulk velocity field in Figure 2(b) shows roll cells consistent with those of a Marangoni instability (though perhaps limited by finite size effects), with a flow field that corresponds to the concentration inhomogeneities (and by implication surface tension inhomogeneities) shown in panel (a).

Despite the existence of roll cells, we find little evidence that a classical Marangoni instability leads to macrovoid formation. For a Marangoni instability to induce macrovoids, the roll cells must be of sufficient magnitude and duration to influence the delayed precipitation event that the polymer film undergoes as solvent/nonsolvent exchange proceeds. However, as exhibited in Figure 2, the magnitude of the concentration inhomogeneities ($|\Delta\phi| \approx 5 \times 10^{-4}$) and velocity of the roll cells ($|\boldsymbol{v}| \approx 10^{-4} R_0/\tau$) are small. Furthermore, we observe that the magnitude of these perturbations decreases with time as the solvent/nonsolvent flux decreases. By $t = 1000$ (data not shown) the magnitude of the concentration inhomogeneities have decreased nearly two orders of magnitude ($|\Delta\phi| \approx 3 \times 10^{-6}$) and the roll cell velocities have shown a similar decline ($|\boldsymbol{v}| \approx 6 \times 10^{-7} R_0/\tau$). Additional results given in the Supporting Information show that increasing the viscosity of the polymer film further decreases the magnitude of these flows. Thus, for a delayed precipitation event the Marangoni flows are inconsequential by the time the polymer film phase separates, and the resulting microstructure is unaffected by their presence.

Although our simulations do not support the hypothesis that a classical Marangoni instability drives the formation of macrovoids, we do find conditions where solutocapillary flows significantly perturb the surface of the polymer film. Using the same model as above (including constant viscosity), we vary the initial polymer film composition so that the delay time before film precipitation is eliminated. Figure 3 shows the ternary phase diagram for the relevant parameters, and the initial conditions of four new simulations alongside the initial condition of the simulation in Figure 2. The initial concentration of the polymer film in the new simulations are very close to (but just outside of) the binodal line, ensuring that the polymer film begins to immediately demix when solvent and nonsolvent are exchanged. Note also that the initial compositions span the polymer-rich and polymer-lean sides of the critical point and include a nearly critical film.

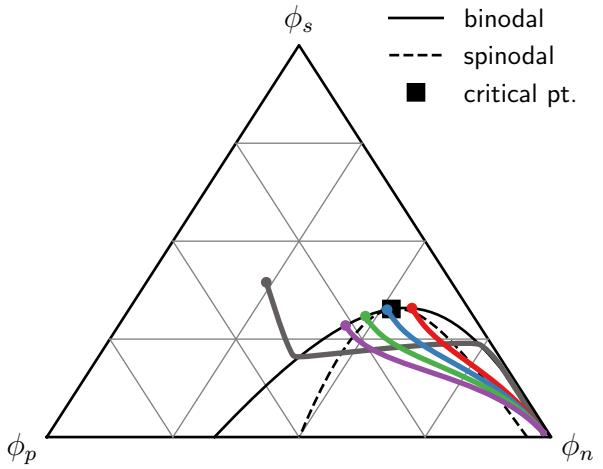

Figure 3: Initial volume fraction profiles and phase diagram for $N = 20$, $\chi = 1.048$ and $\kappa = 2$. A colored dot signifies the initial composition of the polymer film in four different simulations, $\{\phi_p^{(\text{film})}, \phi_n^{(\text{film})}\}$: $\{0.265, 0.450\}$ (purple), $\{0.214, 0.477\}$ (green), $\{0.163, 0.512\}$ (blue), $\{0.112, 0.559\}$ (red). The corresponding colored curves give composition profiles of the four simulations (film, interface and bath) shortly after initiation ($t = 0.1$). The gray curve shows the initial composition profile of data in Figure 2.

Figures 4(a)-(d) shows the polymer volume fraction of the demixing film in the four new simulations as a function of time. Panel

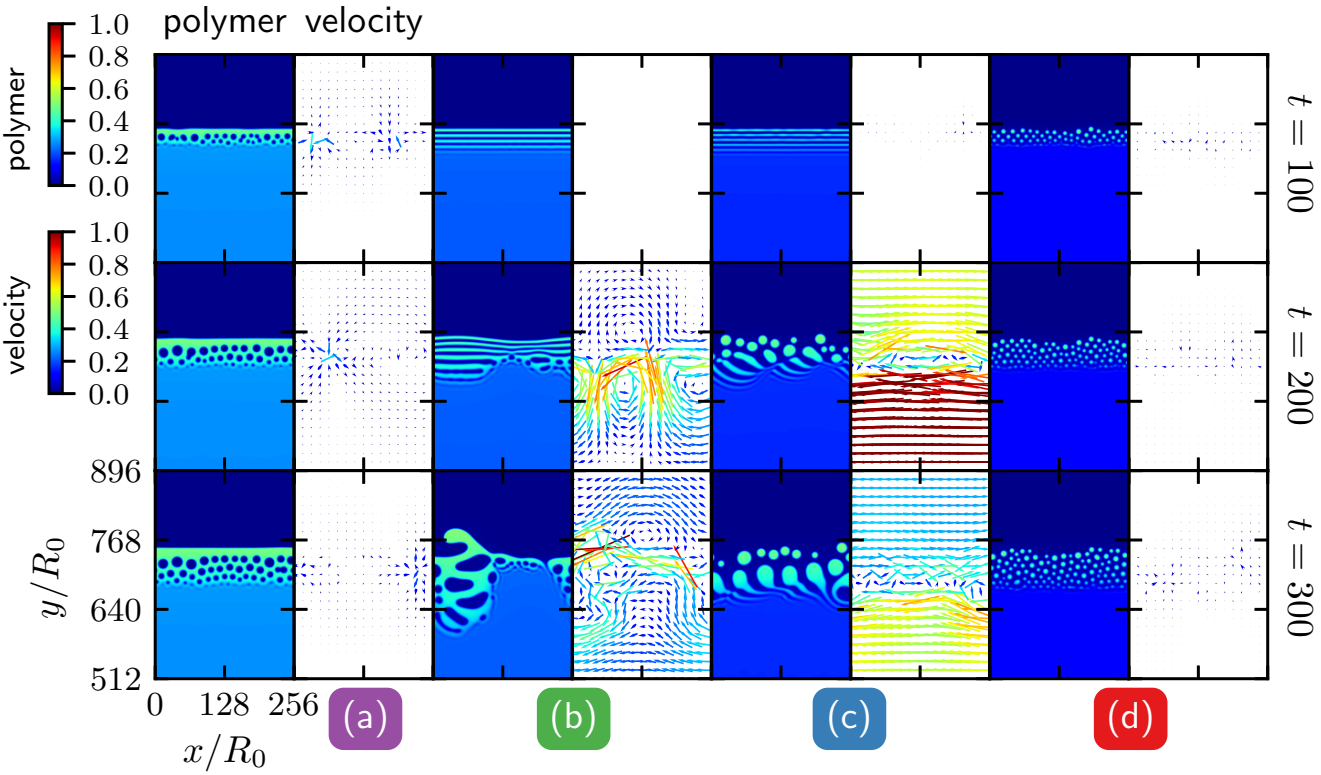

Figure 4: Polymer volume fraction at $t = \{100, 200, 300\}$ corresponding to the different initial film compositions from the phase diagram in Fig 3.

(a) shows a polymer-rich film, which resolves into droplets of nonsolvent in a polymer matrix with a stable interface and relatively little Marangoni flow. Panel (b) shows another polymer-rich film with a higher nonsolvent concentration, which initially shows lamellar bands characteristic of surface-directed spinodal decomposition[20,21]. As time progresses these bands become unstable, and the elongated nonsolvent domains produce strong Marangoni flows, perturbing the interface and the underlying film. The contrast between the simulations in (a) and (b) is reminiscent of the process of coarsening in bulk spinodal decomposition, where the coarsening of nearly bicontinuous morphologies is accelerated by hydrodynamics, but discrete droplet morphologies are not[9].

The initial film concentration in Figure 4(c) is very close to the critical point, and this film also initially has lamellar bands. With increasing time, very strong Marangoni convection coalesces these sheets into large polymer droplets near the top of the film, but the underlying layer still retains a lamellar structure. Interestingly, the polymer domains remain connected to the underlying film, hinting that large pores may be able to form. Finally, panel (d) shows the inverse morphology of panel (a), where a polymer-lean film decomposes into polymer droplets, with velocity magnitudes comparable to the simulations in (a).

It is interesting to note the congruence between the qualitative markers of macrovoid formation listed above and the present simulations: namely the role of hydrodynamics, the sensitivity to the initial film composition and the association with an instantaneous precipitation event. Additionally, there may be interesting connections between the Marangoni flows we observe and pattern-forming solutocapillary instabilities in air-dried, spun-cast polymer films[22–24]. However, despite the circumstantial evidence, none of our simulations clearly show the formation of very large, periodically spaced features that we would classify as macrovoids. Additionally, the omission of physical effects such as thermal fluctuations or vitrification from our model could play an important role in altering the morphologies observed in Fig-

ure 4. Finally, we note that our results are consistent with previous simulation work on both multiphase capillary flow with phase-field[25] and Lattice Boltzmann[26] models and with simulations of phase-separating films in liquid-liquid systems[27] and liquid-air systems[11].

In summary, we have shown that roll cells indicative of a classical Marangoni instability occur in a model of the NIPS process, but are likely too weak to lead to macrovoid formation in a subsequent delayed precipitation process. By contrast, initial bath and film compositions which lead to instantaneous precipitation are coupled to much stronger Marangoni flows that can significantly perturb the surface of the film, especially when the composition is nearly critical. This latter process warrants further investigation as a key mechanism for microstructure formation in NIPS membranes. Additionally, we anticipate that simulations in three dimensions with more sophisticated viscous and viscoelastic models and a more thorough investigation of the role of the initial conditions in the mass transfer process will yield further insight.

Supporting Information Available

- Detailed description of multi-fluid model and methods
- Conditions necessary for a Marangoni instability and justification that NIPS meets these conditions
- Details of the surface tension calculations needed for the prior justification
- A near-critical, pseudo-binary theory of the surface tension
- Variable-viscosity calculations showing roll cells

Acknowledgement

We would like to acknowledge financial support from Asahi Kasei Co. and computational resources from the Center for Scientific Computing from the CNSI, MRL: an NSF MRSEC (DMR-1720256) and NSF CNS-0960316. Additionally we would like to thank Michael Tree for his insights on hydrodynamic stability.

References

(1) Smolders, C. A.; Reuvers, A. J.; Boom, R. M.; Wienk, I. M. Microstructures in phase-inversion membranes. Part 1. Formation of macrovoids. *J. Membr. Sci.* **1992**, *73*, 259–275.

(2) Watanabe, T.; Lopez, C. G.; Douglas, J. F.; Ono, T.; Cabral, J. T. Microfluidic Approach to the Formation of Internally Porous Polymer Particles by Solvent Extraction. *Langmuir* **2014**, *30*, 2470–2479.

(3) Matz, R. The structure of cellulose acetate membranes 1. The development of porous structures in anisotropic membranes. *Desalination* **1972**, *10*, 1–15.

(4) Frommer, M. A.; Messalem, R. M. Mechanism of Membrane Formation. VI. Convective Flows and Large Void Formation during Membrane Precipitation. *Ind. Eng. Chem. Prod. Res. Dev.* **1973**, *12*, 328–333.

(5) Widjojo, N.; Chung, T.-S. Thickness and Air Gap Dependence of Macrovoid Evolution in Phase-Inversion Asymmetric Hollow Fiber Membranes. *Ind. Eng. Chem. Res.* **2006**, *45*, 7618–7626.

(6) Kosma, V. A.; Beltsios, K. G. Macrovoids in solution-cast membranes: Direct probing of systems exhibiting horizontal macrovoid growth. *J. Membr. Sci.* **2012**, *407–408*, 93–107.

(7) Strathmann, H.; Kock, K. The formation mechanism of phase inversion membranes. *Desalination* **1977**, *21*, 241–255.

(8) Prakash, S. S.; Francis, L. F.; Scriven, L. Microstructure evolution in dry–wet cast polysulfone membranes by cryo-SEM: A

hypothesis on macrovoid formation. *J. Membr. Sci.* **2008**, *313*, 135–157.

(9) Tree, D. R.; Delaney, K. T.; Ceniceros, H. D.; Iwama, T.; Fredrickson, G. H. A multi-fluid model for microstructure formation in polymer membranes. *Soft Matter* **2017**, *13*, 3013–3030.

(10) Tanaka, H. Viscoelastic phase separation. *J. Phys.-Condens. Mat.* **2000**, *12*, R207.

(11) Martys, N. S.; Douglas, J. F. Critical properties and phase separation in lattice Boltzmann fluid mixtures. *Phys. Rev. E* **2001**, *63*, 031205.

(12) Akthakul, A.; Scott, C. E.; Mayes, A. M.; Wagner, A. J. Lattice Boltzmann simulation of asymmetric membrane formation by immersion precipitation. *J. Membr. Sci.* **2005**, *249*, 213 – 226.

(13) Wang, X.-L.; Qian, H.-J.; Chen, L.-J.; Lu, Z.-Y.; Li, Z.-S. Dissipative particle dynamics simulation on the polymer membrane formation by immersion precipitation. *J. Membr. Sci.* **2008**, *311*, 251 – 258.

(14) Termonia, Y. Monte Carlo diffusion model of polymer coagulation. *Phys. Rev. Lett.* **1994**, *72*, 3678–3681.

(15) Gompper, G.; Ihle, T.; Kroll, D. M.; Winkler, R. G. *Advanced Computer Simulation Approaches for Soft Matter Sciences III*; Springer Berlin Heidelberg, 2009; pp 1–87.

(16) Ray, R. J.; Krantz, W. B.; Sani, R. L. Linear stability theory model for finger formation in asymmetric membranes. *J. Membr. Sci.* **1985**, *23*, 155–182.

(17) Sternling, C. V.; Scriven, L. E. Interfacial turbulence: Hydrodynamic instability and the marangoni effect. *AIChE Journal* **1959**, *5*, 514–523.

(18) Schwarzenberger, K.; Kllner, T.; Linde, H.; Boeck, T.; Odenbach, S.; Eckert, K. Pattern formation and mass transfer under stationary solutal Marangoni instability. *Adv. Colloid. Interfac.* **2014**, *206*, 344–371.

(19) van de Witte, P.; Dijkstra, P.; van den Berg, J.; Feijen, J. Phase separation processes in polymer solutions in relation to membrane formation. *J. Membrane Sci.* **1996**, *117*, 1–31.

(20) Ball, R. C.; Essery, R. L. H. Spinodal decomposition and pattern formation near surfaces. *J. Phys.: Condens. Matter* **1990**, *2*, 10303–10320.

(21) Jones, R. A. L.; Norton, L. J.; Kramer, E. J.; Bates, F. S.; Wiltzius, P. Surface-directed spinodal decomposition. *Phys. Rev. Lett.* **1991**, *66*, 1326–1329.

(22) Fowler, P. D.; Ruscher, C.; McGraw, J. D.; Forrest, J. A.; Dalnoki-Veress, K. Controlling Marangoni-induced instabilities in spin-cast polymer films: How to prepare uniform films. *Eur. Phys. J. E* **2016**, *39*, 90.

(23) Bormashenko, E.; Pogreb, R.; Stanevsky, O.; Bormashenko, Y.; Stein, T.; Gaisin, V.-Z.; Cohen, R.; Gendelman, O. V. Mesoscopic Patterning in Thin Polymer Films Formed under the Fast Dip-Coating Process. *Macromol. Mater. Eng.* **2005**, *290*, 114–121.

(24) de Gennes, P. Instabilities during the evaporation of a film: Non-glassy polymer + volatile solvent. *Eur. Phys. J. E* **2001**, *6*, 421–424.

(25) Wang, F.; Mukherjee, R.; Selzer, M.; Nestler, B. Numerical study on solutal Marangoni instability in finite systems with a miscibility gap. *Phys. Fluids* **2014**, *26*, 124102.

(26) Stensholt, S.; Øien, A. Lattice Boltzmann simulations of the motion induced by variable surface tension. *Advances in Engineering Software* **2011**, *42*, 944–953.

(27) Zhou, B.; Powell, A. C. Phase field simulations of early stage structure formation during immersion precipitation of polymeric membranes in 2D and 3D. *J. Membr. Sci.* **2006**, *268*, 150–164.

Graphical TOC Entry

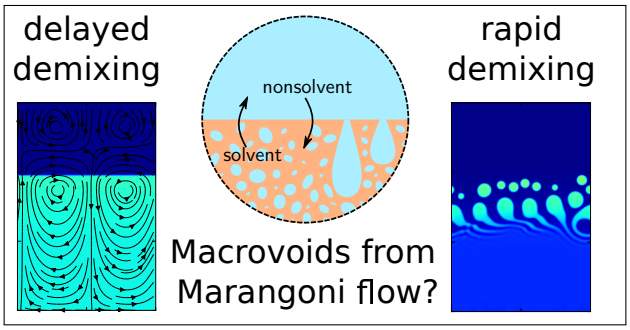

Supporting information for:

Marangoni flows during nonsolvent induced phase separation

Douglas R. Tree,*,† Tatsuhiro Iwama,‡ Kris T. Delaney,¶ Joshua Lee,§ and Glenn Fredrickson‖

†*Chemical Engineering Department, Brigham Young University, Provo, UT 84602*

‡*Asahi Kasei Corporation, 2-1 Samejima, Fuji, Shizuoka 416-8501 Japan*

¶*Materials Research Laboratory, University of California, Santa Barbara, CA 93106-5121*

§*Chemical Engineering Department, University of California, Santa Barbara, CA 93106-5121*

‖*Chemical Engineering Department, Materials Department and Materials Research Laboratory, University of California, Santa Barbara, CA 93106-5121*

E-mail: tree.doug@byu.edu

Description of Multi-fluid Model and Methods

The ternary multi-fluid model was derived using Doi and Onuki's formalism[S1] in a previous publication,[S2] and the final transport equations can be summarized as,

$$\frac{\partial \phi_i}{\partial t} + \boldsymbol{v} \cdot \nabla \phi_i = \nabla \cdot \left[\sum_j^{p,n} M_{ij} \nabla \mu_j \right] \tag{1}$$

$$0 = -\nabla p + \nabla \cdot \left[\eta (\nabla \boldsymbol{v} + \nabla \boldsymbol{v}^T) \right] - \nabla \cdot \boldsymbol{\Pi} \tag{2}$$

$$\nabla \cdot \boldsymbol{v} = 0 \tag{3}$$

where ϕ_i are the volume fractions of the polymer (p), nonsolvent (n) and solvent (s), $\boldsymbol{v}$ is the velocity, M_{ij} are the mobility coefficients, μ_i is the exchange chemical potential of species i, p is the pressure, η is the viscosity, and $\boldsymbol{\Pi}$ is the osmotic stress. Due to incompressibility, the solvent volume fraction, ϕ_s, is not an independent component and is given by,

$$\phi_s = 1 - \phi_p - \phi_n. \tag{4}$$

The chemical potential, μ_i, is given by

$$\mu_i = \frac{k_B T}{b^3} \Big(\frac{\partial f_0}{\partial \phi_i} - \kappa_i \nabla^2 \phi_i \Big) \tag{5}$$

where f_0 is the homogeneous free energy, b is the monomer size, k_B is Boltzmann's constant, T is the absolute temperature and κ_i are gradient coefficients. The homogeneous free energy is given by a ternary Flory–Huggins model,

$$f_0 = \sum_i^{p,n,s} \frac{\phi_i}{N_i} \ln \phi_i + \sum_{i \neq j}^{p,n,s} \chi_{ij} \phi_i \phi_j \tag{6}$$

where N_i parameterize the molecular weight of the components, and χ_{ij} quantify the strength of interaction between species. As mentioned in the main text, in the present study we assume that $N_p = N$, $N_n = N_s = 1$, and $\chi_{pn} = \chi$, $\chi_{ps} = \chi_{ns} = 0$, giving

$$f_0 = \frac{\phi_p}{N} \ln \phi_p + \phi_n \ln \phi_n + \phi_s \ln \phi_s + \chi \phi_p \phi_n. \tag{7}$$

The osmotic stress tensor in Eq. 2 is completely determined by the chemical potential, and its divergence is given by

$$\nabla \cdot \boldsymbol{\Pi} = \phi_n \nabla \mu_n + \phi_p \nabla \mu_p. \tag{8}$$

The mobility coefficients appearing in Eq. 1 are defined as,

$$M_{pp} = \frac{b^3}{\zeta_0}\,\phi_p(1-\phi_p) \tag{9a}$$

$$M_{pn} = M_{np} = -\frac{b^3}{\zeta_0}\,\phi_p\phi_n \tag{9b}$$

$$M_{nn} = \frac{b^3}{\zeta_0}\,\phi_n(1-\phi_n) \tag{9c}$$

where $\zeta_0 = \eta_s b$ is the monomer friction coefficient. The viscosity in Eq. 2 is assumed to be consistent with a Rouse model of polymer solutions,

$$\eta = \eta_s(1 + c\phi_p N_p) \tag{10}$$

where c is a constant that is set to unity. Simulations are conducted with a constant viscosity $\eta = \eta_s$ unless otherwise noted.

Space is discretized in equations 1–3 using pseudo-spectral methods and periodic boundary conditions with $\Delta x = \Delta y = 0.5R_0$. A symmetric initial condition was used to obtain the effective no-flux boundary conditions at $y = 512$ and $y = 1024$ in Figure 3. The diffusion equation (Eq. 1) was solved using a linearly-implicit method, which stabilizes the high-order gradients in the model for large time steps. The momentum and continuity equations (Eq. 2 and Eq. 3) were solved simultaneously using a transverse projection operator, which is explicit in Fourier space. An iterative method is needed to solve the momentum equation when the viscosity depends on concentration. A simple fixed-point method combined with a continuation method and Anderson mixing, gives an efficient solution. All methods were custom-coded using C++ and CUDA for use on a GPGPU. Many more details regarding the model and method can be found in a prior publication.[S2]

Conditions for Marangoni Instability

The Marangoni instability at a liquid-liquid interface was described in a seminal paper by Sternling and Scriven[S3] and exists when (i) a surfactant is diffusing between two liquid phases, and (ii) when the transport of the surfactant is asymmetric between the phases (e.g. there is a diffusivity or viscosity contrast between the two phases[S4]). When this is so, a perturbation gives rise to local surfactant-rich and surfactant-lean inhomogeneities, resulting in a surface-tension gradient and subsequent Marangoni stresses along the interface. These stresses lead to the development of convective roll cells, which are a classical manifestation of the instability.

Without the explicit inclusion of a surfactant, one may dismiss the existence of a Marangoni instability during NIPS, since surface tension gradients are a necessary condition. However this conclusion would

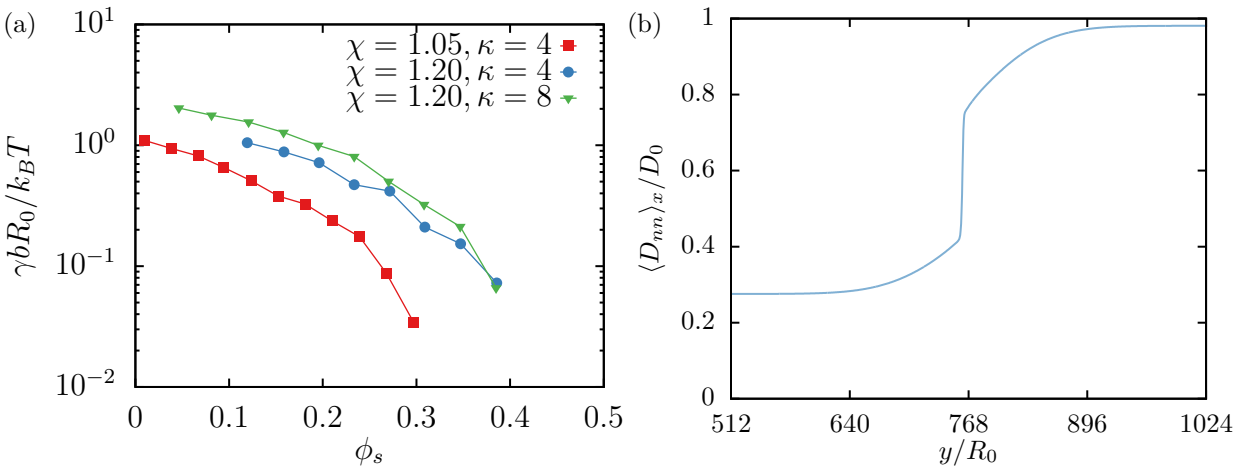

Figure S1: (a) Dimensionless surface tension between a polymer-rich phase and a nonsolvent-rich phase versus average solvent volume fraction for a series of 1D simulations where $N = 20$ and the average polymer and nonsolvent volume fractions $\{\phi_p, \phi_n\}$ are randomly chosen inside the two-phase region of the phase diagram. (b) Nonsolvent-nonsolvent diffusivity for the y-direction (averaged over x) of the NIPS simulation in Figure 2 of the main text. This 2D concentration profile was obtained at $t = 100$ (Rouse time) with thermodynamic parameters $N = 20$, $\chi = 1.048$, $\kappa = 2$, an initial bath composition of $\phi_p^{\text{bath}} = 0.01$, $\phi_n^{\text{bath}} = 0.98$, and an initial film composition of $\phi_p^{\text{film}} = 0.367$ and $\phi_n^{\text{film}} = 0.238$.

be erroneous, because solutal surface tension gradients are possible based solely on the difference between polymer/solvent and polymer/nonsolvent interactions.

To demonstrate that surface tension is a strong function of concentration in our model, we have calculated the surface tension γ between two equilibrated phases using a series of 1D simulations at a variety of N, χ, κ and average concentrations (see below for details of the calculation). Figure S1(a) shows a plot of a dimensionless surface tension, $\gamma b R_0/(k_B T)$ where R_0 is the polymer end-to-end distance, versus solvent concentration for three different values of thermodynamic parameters κ and χ. Two trends are evident from the calculation. First, the surface tension increases when either the polymer-nonsolvent interaction parameter χ increases or the square gradient parameter κ increases. This straightforward result reflects the intuition that an increased enthalpy of interaction or an increased penalty for interfacial contact will result in a higher surface tension.

Second, the surface tension decreases as the average solvent concentration increases. This latter effect can be rationalized by thinking of the solvent as an inert diluent, reducing the high-energy contacts between polymer and nonsolvent. Because χ and κ are constants in a given simulation but solvent concentration is not, we conclude that local variations in solvent concentration are responsible for surface tension inhomogeneities and therefore Marangoni stresses.

In addition to surface tension gradients, Sternling and Scriven's mechanism relies on asymmetric transport between the two phases.[S3,S4] This can be satisfied by either a viscosity contrast or a diffusivity contrast.

In our model, diffusivity is a function of concentration, and asymmetric transport is therefore guaranteed even with constant viscosities. As an example of this, Figure S1(b) shows a plot of the horizontally-averaged nonsolvent component of the mutual diffusion coefficient as a function of y/R_0, the distance normal to the interface between phases. The diffusivity tracks the local concentration,[S2] and is smaller in the film relative to the bath.

Surface Tension Calculations

The surface tension for the multi-fluid model is defined as,[S2,S5,S6]

$$\gamma = \frac{k_B T}{b^3} \int dz \left[\Delta f_0 + \frac{1}{2} \sum_i^{p,n} \kappa_i \left(\frac{d\phi_i}{dz} \right)^2 \right] \tag{11}$$

where Δf_0 is the difference between the local Flory–Huggins free energy and the equilibrium value. This difference is defined as

$$\Delta f_0 = f_0 - f_0^{(e)} - [\phi_p - \phi_p^{(e)}]\mu_p^{(e)} - [\phi_n - \phi_n^{(e)}]\mu_n^{(e)} \tag{12}$$

where the superscript "e" denotes an evaluation of the relevant quantity at the equilibrium volume fraction.

The data points in Figure 2 in the main text are obtained by numerically integrating Eq. 11 using a one-dimensional concentration profile obtained from simulation. Equilibrated concentration profiles were obtained by the following procedure:

1. An initial concentration profile was set to an average concentration plus random noise inside the spinodal, and a simulation was run until phase separated domains appeared.

2. This simulation was then terminated (to avoid long coarsening times inherent to 1D simulations), and the values in the α and β phases were used to provide values for an initial profile.

3. A second simulation was then run, using the result of the first as an initial guess, until the profile contained only two interfaces (for the periodic system) and remained stable.

4. The equilibrated profile was then fed to a Numpy/Python script where Eq. 11 was numerically integrated using Simpson's rule. Because the profiles contain two interfaces, the resulting surface tension was divided by two.

An example profile is shown in Figure S2(a), and the corresponding integrand (the surface energy density) is shown in Figure S2(b).

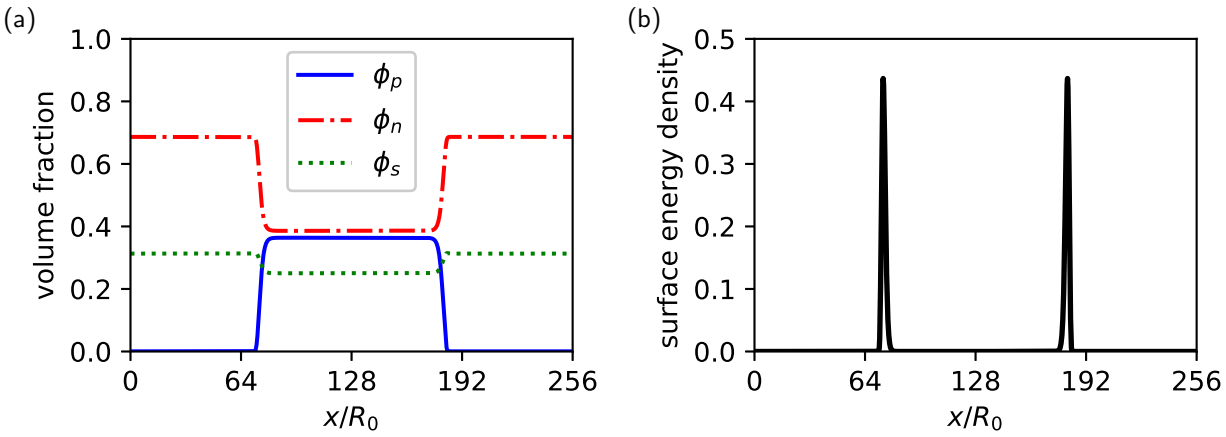

Figure S2: (a) 1D concentration profile for $N = 100$, $\chi = 0.968$, $\kappa = 30$, $\langle\phi_p\rangle = 0.1498$, $\langle\phi_n\rangle = 0.5627$. (b) Surface energy density for the concentration profile.

Table S1: Parameters used to obtain the data in Figure 2 in the main text. $\chi_c^b = \frac{1}{2}\left(\frac{1}{\sqrt{N}} + 1\right)^2$, the critical point for a binary solution of polymer and non-solvent.

N	κ	χ/χ_c^b
1	1	1.2, 1.4, 1.6
2	2	1.4
5	2, 4	1.4
10	1, 2, 4	1.4
20	1, 4, 8	1.2, 1.4, 1.6
50	10, 12, 15, 20, 30	1.4, 1.6
80	15, 20, 30, 40	1.2, 1.4, 1.6
100	20, 30, 40	1.2, 1.4, 1.6

The profile in Figure S2 is just one of many different profiles obtained for different values of N, χ, κ and average concentrations. A table summarizing all of the parameters used to obtain the data in Figure 2 are found in Table S1. Note that this table also appears in a previous publication,[S2] where the same concentration profiles were used to obtain interfacial widths.

A Near-Critical, Pseudo-Binary Theory of the Surface Tension

We show that the surface tension is a function of solvent concentration, providing evidence that Marangoni flows are possible. However, we can go further and show how the surface tension depends on all of the model parameters using a pseudo-binary approximation and scaling theory.

First, it is useful to obtain an approximation to the surface tension for a pseudo-binary solution near the critical point. To do so, we simplify Equations 7, 11 and 12 assuming that the solvent concentration is everywhere constant and equal to its average, $\phi_s = \langle\phi_s\rangle$. We label this the pseudo-binary assumption.

Using this assumption to simplify Eq. 11 leads to

$$\gamma = \frac{k_B T}{b^3} \int dz \left[\Delta f_0 + \kappa_i \left(\frac{d\phi}{dz} \right)^2 \right] \tag{13}$$

where

$$\Delta f_0 = f_0 - f_0^{(e)} - [\phi - \phi^{(e)}]\mu^{(e)} \tag{14}$$

and

$$f_0 = \frac{\phi}{N} \ln \phi + (1 - \phi - \langle \phi_s \rangle) \ln(1 - \phi - \langle \phi_s \rangle) + \langle \phi_s \rangle \ln \langle \phi_s \rangle + \chi \phi (1 - \phi - \langle \phi_s \rangle) \tag{15}$$

with $\phi = \phi_p$.

The logarithms in Eq. 15 make an analytical solution difficult. Furthermore, we showed in a prior work that a near-critical theory did an excellent job describing the interfacial width.[S2] As such, we expand Δf_0 about the critical point,

$$\phi_c = \frac{1 - \langle \phi_s \rangle}{\sqrt{N} + 1} \tag{16}$$

$$\chi_c = \frac{1}{2(1 - \langle \phi_s \rangle)} \left(\frac{1}{\sqrt{N}} + 1 \right)^2. \tag{17}$$

to fourth order giving,

$$\Delta f_0 = \lambda \left[(\Delta \phi)^2 - (\Delta \phi^{(e)})^2 \right]^2 \tag{18}$$

where

$$\Delta \phi = \phi - \phi_c \tag{19}$$

$$\Delta \phi^{(e)} = \phi^{(e)} - \phi_c \tag{20}$$

$$\lambda = \frac{1}{12(1 - \langle \phi_s \rangle)} \frac{(1 + \sqrt{N})^4}{N^{3/2}} \tag{21}$$

and

$$(\Delta \phi^{(e)})^2 = \frac{\chi - \chi_c}{2\lambda}. \tag{22}$$

Equation 13 has a Lagrangian form,[S6] which implies that

$$\left(\frac{d\Delta\phi}{dz} \right)^2 = \frac{\lambda}{\kappa} \left[(\Delta \phi)^2 - (\Delta \phi^{(e)})^2 \right]^2 \tag{23}$$

This can be used to solve for the equilibrium profile, which is a familiar hyperbolic tangent,

$$\Delta\phi = \Delta\phi^{(e)} \tanh\left(-z/l\right) \tag{24}$$

where

$$l = \sqrt{2\kappa}(\chi - \chi_c)^{-1/2} \tag{25}$$

is the interfacial width.[S2]

To find the surface tension, we substitute Eq. 23 into Eq. 13,

$$\gamma = \frac{k_B T}{b^3} \int_{\Delta\phi^{(e)}}^{-\Delta\phi^{(e)}} d\phi \left[2\sqrt{\kappa}(\Delta f_0)^{1/2}\right] \tag{26}$$

$$= \frac{k_B T}{b^3} 2\sqrt{\kappa\gamma} \int_{\Delta\phi^{(e)}}^{-\Delta\phi^{(e)}} d\phi \left[(\Delta\phi)^2 - (\Delta\phi^{(e)})^2\right] \tag{27}$$

and integrate. This gives,

$$\gamma = 8\sqrt{2}\frac{k_B T}{b^3}(1 - \langle\phi_s\rangle)^3 \kappa^{1/2}(\chi - \chi_c)^{3/2} \frac{N^{3/2}}{(1 + N^{1/2})^4} \tag{28}$$

which is the prediction we seek. In the limit that $N \gg 1$, Eq. 28 reduces to

$$\gamma = 8\sqrt{2}\frac{k_B T}{b^3}(1 - \langle\phi_s\rangle)^3 \kappa^{1/2}(\chi - \chi_c)^{3/2} N^{-1/2} \tag{29}$$

which gives a scaling of $\gamma \sim N^{-1/2}(\chi - \chi_c)^{3/2}$, which was previously reported by Widom for a mean-field model near a critical point.[S5,S7]

Figure S3 shows that our data is in excellent agreement with the pseudo-binary theory. Panel (a) shows a representative spinodal, critical line for $N = 20$ alongside part of the data in Table S1. (The data shown in Figure S3(a), correspond to those in Figure 2 of the main text.) Panel (b) is a plot of the normalized surface tension, $\gamma/\gamma_{\text{ref}}$ versus the quench depth, $\chi - \chi_c$, where the reference surface tension

$$\gamma_{\text{ref}} = 8\sqrt{2}\,\frac{k_B T}{b^3}\,\frac{N^{3/2}\kappa^{1/2}(1 - \langle\phi_s\rangle)^3}{(1 + \sqrt{N})^4} \tag{30}$$

contains all of the terms in Eq. 28, except the dependence on the χ-parameter. For completeness, panel (c) also shows a plot of the interfacial width versus $\chi - \chi_c$, similar to a plot produced in a previous paper characterizing our model.[S2] The collapse and quantitative agreement of the data Eq. 28 and Eq. 25 strongly supports the conclusion that the near-critical, pseudo-binary theory provides a satisfactory explanation of

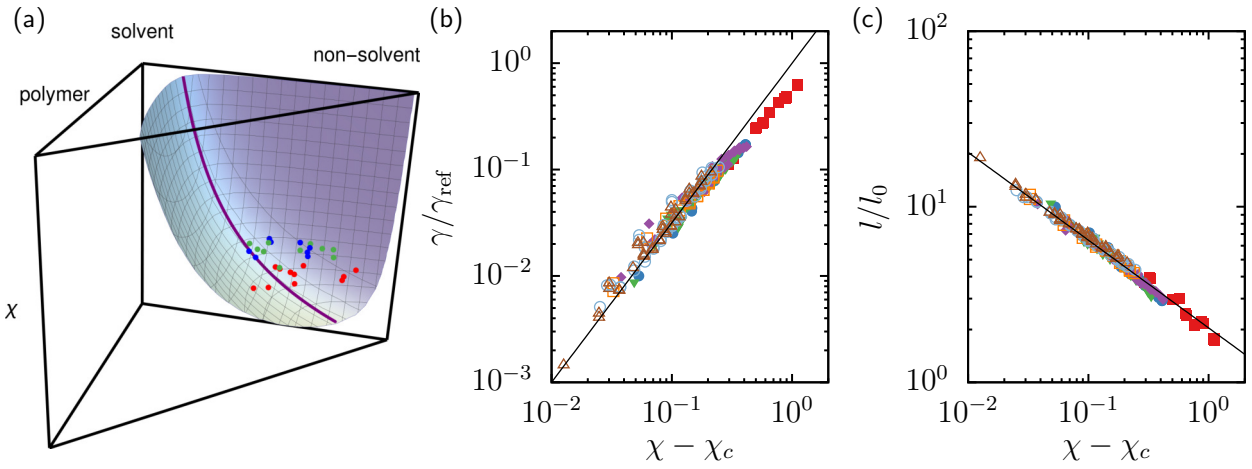

Figure S3: (a) Plot of the spinodal surface and critical line for $N = 20$. Data points at different average concentrations for $N = 20$ and $\{\chi, \kappa\} = \{1.05, 4\}$[red], $\{1.20, 4\}$[green], $\{1.20, 8\}$[blue] are shown, providing an example of the scope of the data contained in the other panels. (b) Normalized surface tension versus quench depth for equilibrated 1D simulations with $N = 1$ (filled red squares), 5 (filled blue circles), 10 (filled green triangles), 20 (filled purple diamonds), 50 (open orange squares), 80 (open blue circles) and 100 (open brown triangles), and a variety of values of κ, χ and average concentrations (see Table S1). The line is $(\chi - \chi_c)^{3/2}$. Note that no fitting parameters have been used. (c) Plot of the interfacial width for the same simulations as panel (b). The line is $(\chi - \chi_c)^{-1/2}$, and again, no fitting parameters have been used.

the 1D data.

Variable-Viscosity Roll Cells

Figure S4 shows the nonsolvent volume fraction, bulk velocity and volume fraction deviation as a function of space for two different 2D simulations of NIPS. The top figure in panel (a), shows a simulation with $\eta = \eta_s$, the lower figure in panel (b) gives a simulation with a viscosity that obeys Eq. 10. Both show qualitatively similar behavior, exhibiting the beginning of diffusive exchange of solvent and nonsolvent in the left-most frame, showing roll cells in the center frame, and displaying local inhomogeneities along the interface in the frame on the right.

Despite the similarities, the roll-cell velocity is approximately an order of magnitude smaller in the variable-viscosity simulation ($\boldsymbol{v}_{\max} = 1.1 \times 10^{-5}$) compared to the constant-viscosity simulation ($\boldsymbol{v}_{\max} = 7.3 \times 10^{-5}$). This decrease in velocity is due to the viscosity difference, not a difference in the magnitude of the concentration inhomogeneity. In fact, while similar in magnitude, the concentration inhomogeneity in the variable-viscosity simulation, $\max(\Delta\phi_n) = 2.8 \times 10^{-4}$, is slightly larger than the constant-viscosity simulation, $\max(\Delta\phi_n) = 1.7 \times 10^{-4}$.

Our observation of a smaller magnitude velocity in the variable-viscosity simulation may seem counter-intuitive, since Sternling and Scriven originally reported that a viscosity contrast would increase the magni-

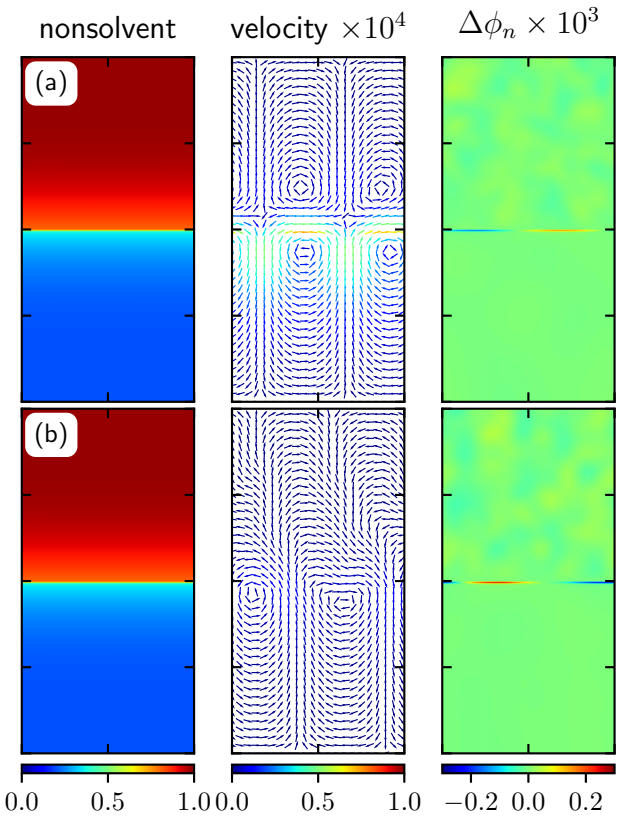

Figure S4: (a) Nonsolvent volume fraction, bulk velocity and volume fraction deviation ($\Delta\phi_n = \phi_n - \langle\phi_n\rangle_x$) at $t = 100$ for a 2D simulation of NIPS with thermodynamic parameters $N = 20$, $\chi = 1.048$, $\kappa = 2$, an initial bath composition of $\phi_p^{\text{bath}} = 0.01$, $\phi_n^{\text{bath}} = 0.98$, and an initial film composition of $\phi_p^{\text{film}} = 0.495$ and $\phi_n^{\text{film}} = 0.204$. The viscosity is everywhere equal to η_s. (b) The same quantities and parameters as the above panel except $\eta = \eta_s(1 + \phi_p N)$.

tude of the roll-cell velocity.[S3] However, unlike ours, Sternling and Scriven's model includes inertial terms, and their analysis assumes an exogenous velocity perturbation of equal magnitude in both phases. By assuming a velocity perturbation, their model implicitly assumes that the concentration inhomogeneity will be greater for a higher viscosity fluid.

By contrast, in our inertia-less model, velocities are slaved to concentrations,[S2] and no such velocity perturbation is possible. Instead, we use a concentration perturbation which has the same magnitude in both simulations. The resulting velocity fields are then inversely scaled by the viscosity, with the large viscosity fluid giving the smaller magnitude velocity field.

References

(S1) Doi, M.; Onuki, A. Dynamic coupling between stress and composition in polymer solutions and blends. *J. Phys. II France* **1992**, *2*, 1631–1656.

(S2) Tree, D. R.; Delaney, K. T.; Ceniceros, H. D.; Iwama, T.; Fredrickson, G. H. A multi-fluid model for microstructure formation in polymer membranes. *Soft Matter* **2017**, *13*, 3013–3030.

(S3) Sternling, C. V.; Scriven, L. E. Interfacial turbulence: Hydrodynamic instability and the marangoni effect. *AIChE Journal* **1959**, *5*, 514–523.

(S4) Schwarzenberger, K.; Kllner, T.; Linde, H.; Boeck, T.; Odenbach, S.; Eckert, K. Pattern formation and mass transfer under stationary solutal Marangoni instability. *Adv. Colloid. Interfac.* **2014**, *206*, 344–371.

(S5) Cahn, J. W.; Hilliard, J. E. Free Energy of a Nonuniform System. I. Interfacial Free Energy. *J. Chem. Phys.* **1958**, *28*, 258–267.

(S6) Broseta, D.; Fredrickson, G. H.; Helfand, E.; Leibler, L. Molecular weight and polydispersity effects at polymer-polymer interfaces. *Macromolecules* **1990**, *23*, 132–139.

(S7) Widom, B. Scaling of the surface tension of phase-separated polymer solutions. *J. Stat. Phys.* **1988**, *53*, 523–529.